7. ANKARA INTERNATIONAL AEROSPACE CONFERENCE AIAC-2013-026
11-13 September 2013 - METU, Ankara TURKEY

A TIME DEPENDENT FULLY COUPLED FLUID-STRUCTURE INTERACTION ALGORITHM

Ali Eken* and Mehmet Sahin†
Istanbul Technical University
Istanbul, Turkey

ABSTRACT

A time dependent numerical algorithm has been developed for the numerical simulation of fluid structure interaction problems. The incompressible Navier-Stokes equations are discretized using an Arbitrary Lagrangian-Eulerian (ALE) formulation based on the side-centered unstructured finite volume method. The side-centered arrangement of the primitive variables leads to a stable numerical scheme and it does not require any $ad\text{-}hoc$ modifications in order to enhance the pressure-velocity coupling. A special attention is also given to satisfy the discrete geometric conservation law (DGCL). In order to account for large structural displacements, the structural behaviour of the solid domain is governed by the Saint Venant-Kirchhoff material model. The Galerkin finite element method is used to discretize the nonlinear elasticity equations within the structure domain. The resulting nonlinear algebraic equations are solved in a fully coupled form using the restricted additive Schwarz method with the flexible GMRES(m) algorithm. The implementation of the fully coupled preconditioned iterative solvers is based on the PETSc library for improving the efficiency of the parallel code. The present numerical algorithm is validated for a Newtonian fluid interacting with an elastic rectangular bar behind a circular cylinder, and a pulsatile flow in a flexible tube, which mimics the case of pulsatile blood flow through elastic arteries.

INTRODUCTION

The FSI problem is mainly characterized by the mutual interaction between a movable or deformable structure with an internal or surrounding fluid flow. Typical examples in engineering applications involve aeroelastic phenomena like flutter of aircraft wings or turbine blades and tail buffeting, inflation of parachutes or airbags, design of sails or tent structures, structural effect of strong wind on bridges and tall buildings, and many others. On the other hand, much of the work in biomedical applications include blood flow in the veins and arteries, dynamics of heart valves, deformations and aggregations of blood cells. Accurate prediction of fluid-structure interactions is crucial for many engineering structures in order to avoid potential aeroelastic/hydroelastic instabilities, which may cause catastrophic failures of the structure.

There are mainly two approaches for the modeling of fluid-structure interaction problems: partitioned (segregated) [Degroote and Vierendeels, 2011] or fully coupled (monolithic)[Muddle et al., 2012] methods. In the partitioned approach, separate solvers are used for the fluid and structure subproblems. The main advantage of the partitioned approach is the ability to reuse existing solvers, which allows the application of different, possibly more efficient computational methods specifically developed for either the fluid or the structure subproblems. Both explicit or implicit methods can be used in order to couple the fluid and structure solvers in partitioned procedures. In explicit partitioned methods, which are also known as loosely or weakly coupled methods, typically a fixed point (Picard) iteration is employed to obtain a coupled solution. Although the implementation of this method is relatively easy, it does, however, suffer some serious drawbacks. The fixed point iterations tend to converge slowly if at all, and the iterations may diverge in the presence of strong

*GRA in Aeronautical Engineering Department, Email: ekena@itu.edu.tr
†Assoc. Prof. in Astronautical Engineering Department, Email: msahin@itu.edu.tr

fluid-solid interactions due to a comparable fluid-to-solid density ratio, which is encountered frequently in FSI problems in biomechanics. In addition, weakly coupled partitioned methods can not satisfy the incompressibility constraint of the fluid during standard alternating FSI iterations where the fluid domain is entirely enclosed by Dirichlet boundary conditions. For strong coupling in partitioned procedures, on the contrary, several fluid and structure computations are performed in a single time-step until a satisfactory convergence tolerance is reached. This approach, however requires costly sub-iterations, and the sub-iteration convergence may not be guaranteed. In a fully coupled (monolithic) approach, the fluid and structure equations are discretised and solved simultaneously as a single equation system for the entire problem. However, this requires an efficient numerical technique for the solution of a large system of coupled nonlinear algebraic equations, which poses the major challenge of monolithic FSI approaches, especially in large scale problems. Although monolithic solver are believed to be too expensive for use in large-scale problems, more recent studies [Küttler et al., 2010] demonstrates that monolithic solvers are competitive even in test cases with very weak FSI, where their segregated counterparts do not suffer from any convergence problems. In this context, Muddle et al. [Muddle et al., 2012] presented a block preconditioner for the efficient solution of the linear systems by Krylov subspace solvers. Behr and Tezduyar [Behr and Tezduyar, 1994] presented solution strategies for large-scale flow simulations and Johnson and Tezduyar [Johnson and Tezduyar, 1994] proposed mesh update strategies in parallel computations. Gee et al. [Gee et al., 2011] applied an algebraic multigrid technique to the entire fluid-structure interaction system of equations. Barker and Cai [Barker and Cai, 2010] developed a scalable parallel finite element solver for the simulation of blood flow in compliant arteries using scalable Newton-Krylov algorithms preconditioned with an overlapping restricted additive Schwarz method.

One of the most well-known methods used to capture the interaction between structure and fluid is the Arbitrary Lagrangian Eulerian (ALE) method as described in [Hirt et al., 1974]. In the ALE method, the mesh follows the interface between the fluid and solid boundary and the governing equations are discretized on a moving mesh. This differs from the standard Eulerian formulation in a way that the mesh movement has to fulfill special conditions in order to maintain the accuracy and the stability of the time integration scheme. This condition is satisfied by the enforcement of the so-called geometric conservation law (GCL) as coined by [Thomas and Lombard, 1979]. The ALE approach was subsequently adopted within the finite element context to solve free surface problems of incompressible viscous fluid flow [Hughes et al., 1981]. In the case of an FSI problem, the deformable fluid-structure interface is taken into account and the fluid points at the fluid-solid interface are moved in a Lagrangian way [Donea et al., 1982].

This article presents a new numerical algorithm based on the ALE formulation for a fully coupled solution of the FSI problems where the fluid is modeled by the incompressible Navier-Stokes equations and the structure is modeled by the St. Venant-Kirchhoff model. The governing equations of the fluid domain are discretized using an Arbitrary Lagrangian-Eulerian (ALE) formulation based on the side-centered unstructured finite volume method where the velocity vector components are defined at the mid-point of each cell face while the pressure is defined at the element centroid. The present arrangement of the primitive variables leads to a stable numerical scheme and it does not require any $ad\text{-}hoc$ modifications in order to enhance the pressure-velocity coupling. The most appealing feature of the present finite volume approach is that it leads to the classical five-point Laplace operator for the pressure Poisson equation as in the classical MAC scheme [Harlow and Welch, 1965] which is very important for the efficient solution of the large-scale FSI problems. In the present work, a special attention is given to satisfy the continuity equation exactly within each element and the summation of the continuity equations can be exactly reduced to the domain boundary, which is important for the global mass conservation. The mesh deformation within the fluid domain is achieved by using an algebraic approach based on the minimum distance function at each time level while avoiding re-meshing in order to enhance numerical robustness. The deformation of the solid domain is governed by the constitutive laws for the nonlinear Saint Venant-Kirchhoff material and the classical Galerkin finite element is used to discretize the governing equations in a Lagrangian frame. Newmark type generalized-α method is employed for the time integration of the solid dynamic equilibrium equation. The solution of the resulting fully coupled system is based on the restricted additive Schwarz method with the flexible GMRES(m) algorithm. Within each partitioned sub-domains, an incomplete ILU(k) algorithm coupled with the reverse Cuthill-McKee ordering is used. In order to avoid the zero block due to the divergence-free constrain, the original system is multiplied by an upper triangular right preconditioner, which results in a scaled discrete Laplacian instead of the zero block in the original system. For computational efficiency, the implementation of the iterative solver is based on the PETSc library [Balay et al., 2012]. The computational fluid-structure domain is partitioned into a set of sub-domains using the METIS library [Karypis and Kumar, 1998].

The first part of this paper provides some details on the present FSI algorithm with detailed discussions on the iterative solvers. Subsequently, the proposed method is validated for two reference FSI benchmark problems: A steady Newtonian fluid interacting with an elastic bar behind a cylinder, and a pulsatile flow in a flexible

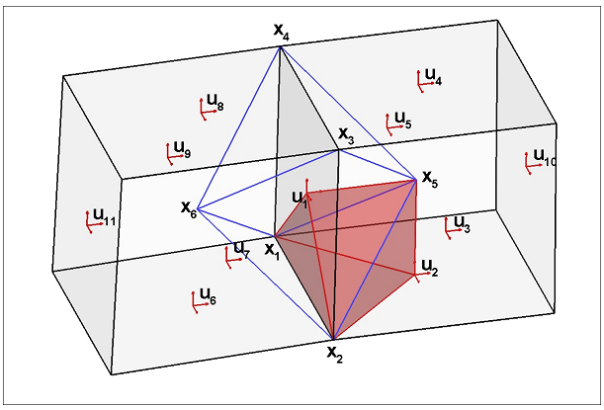

Figure 1: Three-dimensional unstructured mesh with a dual control volume (Ω_d) (blue lines) and a covolume (Ω_c) used to compute the gradients at the dual volume face $\mathbf{A}_{125}$ (red volume).

tube, which simulates the case of pulsatile blood flow through elastic arteries. Finally the concluding remarks are provided addressing the future work to further improve the present FSI algorithm.

MATHEMATICAL and NUMERICAL FORMULATION

Fluid model

The integral form of the incompressible Navier-Stokes equations that govern the motion of an arbitrary moving control volume $\Omega(t)$ with boundary $\partial\Omega(t)$ can be written in the Cartesian coordinate system in dimensionless form as follows: the momentum equations

$$Re\int_{\Omega_d}\frac{\partial \mathbf{u}}{\partial t}dV + Re\oint_{\partial\Omega_d}\left[\mathbf{n}\cdot(\mathbf{u}-\dot{\mathbf{x}})\right]\mathbf{u}dS + \oint_{\partial\Omega_d}\mathbf{n}pdS = \oint_{\partial\Omega_d}\mathbf{n}\cdot\nabla\mathbf{u}dS \tag{1}$$

the continuity equation

$$-\oint_{\partial\Omega_e}\mathbf{n}\cdot\mathbf{u}\,dS = 0 \tag{2}$$

In these equations, V is the control volume, S is the control volume surface area, $\mathbf{n}$ represents the outward normal vector, $\mathbf{u}$ represents the local fluid velocity vector, $\dot{\mathbf{x}}$ represents the grid velocity, p is the pressure and Re is the dimensionless Reynolds number. The local fluid velocity vector components are defined at the mid-point of each face, while the pressure is defined at the element centroids. The above continuity equation is discretized within each hexahedral element Ω_e, meanwhile the momentum equations are discretized over the dual finite volume Ω_d as shown Figure 1. The dual finite volume Ω_d is constructed by connecting the element centroids to the common vertices shared by the both hexahedral elements. On the other hand, the covolume Ω_c is constructed on the dual volume triangular faces in order to compute the velocity vector component gradients at the dual volume faces.

Solid Model

The structural behaviour of solid domain is governed by the following conservation of momentum in the Lagrangian framework where the material derivative becomes a partial derivative with respect to time

$$\rho\frac{\partial^2\mathbf{d}}{\partial \mathrm{t}^2} = \nabla\cdot\boldsymbol{\sigma}_s + \rho\mathbf{b} \tag{3}$$

where ρ is the solid material density, $\mathbf{d}$ is the displacement vector, σ_s is the Cauchy stress tensor and $\mathbf{b}$ is the body forces. The material is defined by the Cauchy stress tensor using the following constitutive law for the Saint Venant-Kirchhoff material:

$$\mathbf{S} = J\mathbf{F}^{-1}\sigma_s\mathbf{F}^{-\top} \tag{4}$$

$$\mathbf{F} = (\mathbf{I}+\nabla\mathbf{d}) \tag{5}$$

$$\mathbf{E} = \frac{1}{2}(\mathbf{F}^{\top}\mathbf{F}-\mathbf{I}) \tag{6}$$

$$\mathbf{S} = \lambda\mathrm{trace}(\mathbf{E})\mathbf{I}+2\mu\mathbf{E} \tag{7}$$

$$\mathbf{\Pi} = \mathbf{F}\mathbf{S} \tag{8}$$

where $\mathbf{S}$ is the second Piola-Kirchhoff stress tensor, $\mathbf{F}$ is the deformation gradient tensor, $J = det(\mathbf{F})$ is the deformation gradients determinant, $\mathbf{E}$ is the Green-Lagrange strain tensor, $\mathbf{\Pi}$ is the non-symmetric first Piola-Kirchhoff stress tensor and λ and μ are the material Lame's constants. Then the equation of motion with respect to the initial configuration is given by

$$\rho_0 \frac{\partial^2 \mathbf{d}}{\partial \mathrm{t}^2} = \nabla \cdot \mathbf{\Pi} + \rho_0 \mathbf{b} \tag{9}$$

where ρ_0 is the solid material density per unit undeformed volume.

Interface Conditions

A main requirement for the coupling schemes is to fulfill two coupling conditions: the kinematic and the dynamic continuity across the fluid-solid interface at all times. The kinematic boundary conditions on the fluid-structue interface is driven by requiring continuity of the velocity

$$\mathbf{u} = \dot{\mathbf{d}} \tag{10}$$

while the dynamic condition means that the following equilibrium equation holds for the surface traction at the common fluid-structure interaction boundary

$$\sigma_s \mathbf{n}_s = -\sigma_f \mathbf{n}_f \tag{11}$$

where $\mathbf{n}_s$ and $\mathbf{n}_f$ denote the outward-pointing unit normal on the fluid-structure boundary, viewed from the structure and fluid domains, respectively. The parameter σ_s represents the Cauchy stress tensor of the solid domain and σ_f is the stress tensors in the case of an incompressible Newtonian fluid. The constitutive relation for the fluid stress tensor is given by

$$\sigma_f = -p\mathbf{I} + \mu_f(\nabla \mathbf{u} + \nabla \mathbf{u}^\top) \tag{12}$$

where μ_f is the fluid dynamic viscosity.

Numerical Discretization of ALE Formulation for Fluid Domain

The momentum equations along the $x-$, $y-$ and $z-$directions are discretized over the dual finite volume Ω_d shown in Figure 1 and the dual volume involves only the right and left elements that share the common face where the components of the velocity vector are discretized. The discrete contribution from the right cell shown in Figure 1 is given below for each term of the momentum equation along the $x-$direction.

The time derivative

$$\frac{3Re}{2}\left[\frac{3u_1^{n+1}}{4\Delta t} + \frac{\sum_i u_i^{n+1}}{6\cdot 4\Delta t}\right] V_{12345}^{n+1} - \frac{4Re}{2}\left[\frac{3u_1^{n}}{4\Delta t} + \frac{\sum_i u_i^{n}}{6\cdot 4\Delta t}\right] V_{12345}^{n} + \frac{Re}{2}\left[\frac{3u_1^{n-1}}{4\Delta t} + \frac{\sum_i u_i^{n-1}}{6\cdot 4\Delta t}\right] V_{12345}^{n-1}$$
$$\text{with} \quad i = 1,2,3,4,5,10 \tag{13}$$

The convective term due to fluid motion

$$\begin{aligned} &+ \quad Re\left[\mathbf{u}_{125}^{n+1}\cdot\mathbf{A}_{125}^{n+1}\right]u_{125}^{n+1} + Re\left[\mathbf{u}_{235}^{n+1}\cdot\mathbf{A}_{235}^{n+1}\right]u_{235}^{n+1} \\ &+ \quad Re\left[\mathbf{u}_{345}^{n+1}\cdot\mathbf{A}_{345}^{n+1}\right]u_{345}^{n+1} + Re\left[\mathbf{u}_{415}^{n+1}\cdot\mathbf{A}_{415}^{n+1}\right]u_{415}^{n+1} \end{aligned} \tag{14}$$

The convective term due to mesh motion

$$\begin{aligned} &- \quad Re\left[\dot{\mathbf{x}}_{125}^{n+1}\cdot\mathbf{A}_{125}^{n+1}\right]u_{125}^{n+1} - Re\left[\dot{\mathbf{x}}_{235}^{n+1}\cdot\mathbf{A}_{235}^{n+1}\right]u_{235}^{n+1} \\ &- \quad Re\left[\dot{\mathbf{x}}_{345}^{n+1}\cdot\mathbf{A}_{345}^{n+1}\right]u_{345}^{n+1} - Re\left[\dot{\mathbf{x}}_{415}^{n+1}\cdot\mathbf{A}_{415}^{n+1}\right]u_{415}^{n+1} \end{aligned} \tag{15}$$

The pressure term

$$\begin{aligned} &\left[\frac{p_1+p_2+p_5}{3}\right]^{n+1}\mathbf{A}_{125}^{n+1}\cdot\mathbf{i} + \left[\frac{p_2+p_3+p_5}{3}\right]^{n+1}\mathbf{A}_{235}^{n+1}\cdot\mathbf{i} \\ &+\left[\frac{p_3+p_4+p_5}{3}\right]^{n+1}\mathbf{A}_{345}^{n+1}\cdot\mathbf{i} + \left[\frac{p_4+p_1+p_5}{3}\right]^{n+1}\mathbf{A}_{415}^{n+1}\cdot\mathbf{i} \end{aligned} \tag{16}$$

The viscous term

$$
\begin{aligned}
- & \left[\left(\frac{\partial u}{\partial x}\right)_{125}^{n+1}\mathbf{A}_{125}^{n+1}\cdot\mathbf{i}+\left(\frac{\partial u}{\partial y}\right)_{125}^{n+1}\mathbf{A}_{125}^{n+1}\cdot\mathbf{j}+\left(\frac{\partial u}{\partial z}\right)_{125}^{n+1}\mathbf{A}_{125}^{n+1}\cdot\mathbf{k}\right] \\
- & \left[\left(\frac{\partial u}{\partial x}\right)_{235}^{n+1}\mathbf{A}_{235}^{n+1}\cdot\mathbf{i}+\left(\frac{\partial u}{\partial y}\right)_{235}^{n+1}\mathbf{A}_{235}^{n+1}\cdot\mathbf{j}+\left(\frac{\partial u}{\partial z}\right)_{235}^{n+1}\mathbf{A}_{235}^{n+1}\cdot\mathbf{k}\right] \\
- & \left[\left(\frac{\partial u}{\partial x}\right)_{345}^{n+1}\mathbf{A}_{345}^{n+1}\cdot\mathbf{i}+\left(\frac{\partial u}{\partial y}\right)_{345}^{n+1}\mathbf{A}_{345}^{n+1}\cdot\mathbf{j}+\left(\frac{\partial u}{\partial z}\right)_{345}^{n+1}\mathbf{A}_{345}^{n+1}\cdot\mathbf{k}\right] \\
- & \left[\left(\frac{\partial u}{\partial x}\right)_{415}^{n+1}\mathbf{A}_{415}^{n+1}\cdot\mathbf{i}+\left(\frac{\partial u}{\partial y}\right)_{415}^{n+1}\mathbf{A}_{415}^{n+1}\cdot\mathbf{j}+\left(\frac{\partial u}{\partial z}\right)_{415}^{n+1}\mathbf{A}_{415}^{n+1}\cdot\mathbf{k}\right]
\end{aligned}
\tag{17}
$$

where V_{12345} is the volume of the pyramid between the points $\mathbf{x}_1$, $\mathbf{x}_2$, $\mathbf{x}_3$, $\mathbf{x}_4$ and $\mathbf{x}_5$ shown in Figure 1, $\mathbf{A}_{125}$, $\mathbf{A}_{235}$, $\mathbf{A}_{345}$ and $\mathbf{A}_{415}$ are the area vectors of the dual volume triangular surfaces, Δt is the time step, the values $\mathbf{u}_{125}$, $\mathbf{u}_{235}$, $\mathbf{u}_{345}$ and $\mathbf{u}_{415}$ are the velocity vectors defined at the mid-point of each dual volume area and p_1, p_2, p_3, p_4 and p_5 are the pressure values at the points $\mathbf{x}_1$, $\mathbf{x}_2$, $\mathbf{x}_3$, $\mathbf{x}_4$ and $\mathbf{x}_5$, respectively. However, the pressure values are known only at the element centroids and the pressure values at $\mathbf{x}_1$, $\mathbf{x}_2$, $\mathbf{x}_3$ and $\mathbf{x}_4$ have to be computed. To compute the pressure at $\mathbf{x}_1$, as an example, a second-order Taylor series expansion can be written as

$$
p_i = p_1 + \frac{\partial p}{\partial x}\,|_{\mathbf{x}=\mathbf{x}_1}\,(x_{c,i}-x_1) + \frac{\partial p}{\partial y}\,|_{\mathbf{x}=\mathbf{x}_1}\,(y_{c,i}-y_1) + \frac{\partial p}{\partial z}\,|_{\mathbf{x}=\mathbf{x}_1}\,(z_{c,i}-z_1) \quad \text{with} \quad i=1,2,..,m \tag{18}
$$

where m represents the number of the neighboring hexahedral elements connected to the point $\mathbf{x}_1$ and $\mathbf{x}_{c,i}$ corresponds to the neighboring element centroids. This overdetermined system of linear equations may be solved in a least square sense using the normal equation approach, in which both sides are multiplied by the transpose. The modified system is solved to compute the pressure and its gradients using the singular value decomposition provided by the Intel Math Kernel Library in order to avoid the numerical difficulties associated with solving linear systems with near rank deficiency. In a similar manner, the $u-$velocity component values at $\mathbf{x}_1$, $\mathbf{x}_2$, $\mathbf{x}_3$ and $\mathbf{x}_4$ are computed using the same approach. To compute the $u-$velocity component at $\mathbf{x}_1$,

$$
u_i = u_1 + \frac{\partial u}{\partial x}\,|_{\mathbf{x}=\mathbf{x}_1}\,(x_{f,i}-x_1) + \frac{\partial u}{\partial y}\,|_{\mathbf{x}=\mathbf{x}_1}\,(y_{f,i}-y_1) + \frac{\partial u}{\partial z}\,|_{\mathbf{x}=\mathbf{x}_1}\,(z_{f,i}-z_1) \quad \text{with} \quad i=1,2,..,l \tag{19}
$$

where l represent the number of the faces connected to the point $\mathbf{x}_1$ and $\mathbf{x}_{f,i}$ corresponds to the face mid-points. The overdetermined system of linear equations is also solved in a least square sense as before and the computed $u-$velocity components are used to compute the velocity gradients defined at the mid-point of each dual volume triangular faces using the Green-Gauss theorem:

$$
\nabla u = \frac{\partial u}{\partial x}\mathbf{i} + \frac{\partial u}{\partial y}\mathbf{j} + \frac{\partial u}{\partial z}\mathbf{k} = \frac{1}{V_c}\oint_{\partial\Omega_c} u d\mathbf{A} \tag{20}
$$

where V_c covolume consists of two tetrahedral elements that share the same dual volume triangular surface area with their fourth vertices located at the midpoint of the hexahedral element faces as illustrated in Figure 1. The right-hand side of the equations (20) is evaluated using the mid-point rule on each of the covolume faces.

The convective velocity vector components u_{125}, u_{235}, u_{345} and u_{415} are computed at the mid-point of the dual volume triangular surfaces using the least square upwind interpolations [Barth, 1991; Anderson and Bonhaus, 1994]. As an example,

$$
u_{125} = \beta\left[u_1 + \nabla u_1\cdot(\mathbf{x}_{125}-\mathbf{x}_{f,1})\right] + (1-\beta)\left[u_2 + \nabla u_2\cdot(\mathbf{x}_{125}-\mathbf{x}_{f,2})\right] \tag{21}
$$

where β is a weight factor determining the type of convection scheme used, ∇u_1 and ∇u_2 are the gradients of velocity components where the u_1 and u_2 velocity components are defined and $\mathbf{x}_{125} = (\mathbf{x}_1+\mathbf{x}_2+\mathbf{x}_5)/3$. For evaluating the gradient terms, ∇u_1 and ∇u_2, a least square procedure is used in which the velocity data is assumed to behave linearly.

To compute the fluxes due to mesh motion, a special attention is given to satisfy the discrete geometric conservation law (DGCL). The DGCL states that the volumetric increment of a moving element must be

equal to the summation of the volumes swept by its surfaces that close the volume. Therefore, the mesh motion flux is evaluated as follows [Geuzaine et al., 2003; Naderi et al., 2010]

$$\dot{\mathbf{x}}_{125}^{n+1} \cdot \mathbf{A}_{125}^{n+1} = \frac{3}{2\Delta t}(\mathbf{x}_{125}^{n+1} - \mathbf{x}_{125}^{n}) \cdot \frac{\left[\mathbf{A}_{125}^{n+1} + \mathbf{A}_{125}^{n}\right]}{2} - \frac{1}{2\Delta t}(\mathbf{x}_{125}^{n} - \mathbf{x}_{125}^{n-1}) \cdot \frac{\left[\mathbf{A}_{125}^{n} + \mathbf{A}_{125}^{n-1}\right]}{2} \tag{22}$$

This approach will ensure that the DGCL is satisfied and the present ALE scheme preserves a uniform flow solution exactly independent of the mesh motion. However, Geuzaine et al. [Geuzaine et al., 2003] showed that the compliance with the DGCL is neither a necessary nor a sufficient condition to preserve its order of time-accuracy established on fixed meshes. Because, the authors indicated by means of truncation error arguments that the linearization of the convective terms in the equation (14) using the values at time level n will drop the accuracy of the numerical scheme to first-order on moving meshes.

In comparison to the staggered methods, the use of the both velocity components significantly simplifies the discretization of the governing equations as well as the implementation of physical boundary conditions. The discretization of the momentum equation along the $y-$ and $z-$direction follows very closely the ideas presented here. It should be noted that the present dual volume surface integrals involve only triangular planar surfaces for the momentum equations which significantly simplify the three-dimensional numerical discretization. The continuity equation (2) is integrated within each hexahedral elements and evaluated using the mid-point rule on each of the element faces

$$-\sum_{i=1}^{6} \left[u^{n+1}A_x\right]_i + \left[v^{n+1}A_y\right]_i + \left[w^{n+1}A_z\right]_i = 0 \tag{23}$$

where $\mathbf{A} = A_x\mathbf{i} + A_y\mathbf{j} + A_z\mathbf{k}$ is the hexahedral element surface area vector and u, v and w are the velocity vector components defined at the mid-point of each hexahedral element face. The discretization of above equations leads to a saddle point problem [M. Benzi and Liesen, 2005] of the form:

$$\begin{bmatrix} A_{11} & 0 & 0 & A_{14} \\ 0 & A_{22} & 0 & A_{24} \\ 0 & 0 & A_{33} & A_{34} \\ A_{41} & A_{42} & A_{43} & 0 \end{bmatrix} \begin{bmatrix} u \\ v \\ w \\ p \end{bmatrix} = \begin{bmatrix} b_1 \\ b_2 \\ b_3 \\ 0 \end{bmatrix} \tag{24}$$

where, A_{11}, A_{22} and A_{33} are the convection diffusion operators, $(A_{14}, A_{24}, A_{34})^\top$ is the pressure gradient operator and (A_{41}, A_{42}, A_{43}) is the divergence operator. It should also be noted that on an uniform Cartesian mesh the multiplication of the matrices $A_{41}A_{14} + A_{42}A_{24} + A_{43}A_{34}$ gives the classical five-point Laplace operator as in the MAC scheme [Harlow and Welch, 1965] which is extremely important for the efficient implementation of the present preconditioned iterative solvers.

Galerkin Finite Element Discretization for Solid Domain

The weak form of the equations can be obtained by multiplying the equation (9) by the test function and integrating over the solid domain

$$\int_{\Omega_e} N_i \rho_0 \frac{\partial^2 \mathbf{d}}{\partial \mathrm{t}^2} dV_0 = \int_{\Omega_e} N_i \left(\nabla \cdot \mathbf{\Pi} + \rho \mathbf{b}\right) dV_0 \tag{25}$$

Integrating by parts one has

$$\int_{\Omega_e} N_i \rho_0 \frac{\partial^2 \mathbf{d}}{\partial \mathrm{t}^2} dV_0 = \int_{\Omega_e} \nabla \cdot (N_i \mathbf{\Pi})\, dV_0 - \int_{\Omega_e} \mathbf{\Pi} \nabla N_i dV_0 + \int_{\Omega_e} N_i \rho_0 \mathbf{b} dV_0 \tag{26}$$

The first term can be related to a surface integral by the divergence theorem and the weak form can be obtained as

$$\int_{\Omega_e} N_i \rho_0 \frac{\partial^2 \mathbf{d}}{\partial \mathrm{t}^2} dV_0 = \oint_{\partial\Omega_e} (N_i \mathbf{\Pi})\, \mathbf{n} dS_0 - \int_{\Omega_e} \mathbf{\Pi} \nabla N_i dV_0 + \int_{\Omega_e} N_i \rho_0 \mathbf{b} dV_0 \tag{27}$$

The displacements at any point in the isoparametric hexahedral element are approximated by a linear combi-

nation of the displacements at the nodal points of the element

$$\left\{ \begin{array}{c} d_x \\ d_y \\ d_z \end{array} \right\} = \left[\begin{array}{cccccccccccc} N_1 & 0 & 0 & N_2 & 0 & 0 & N_3 & 0 & 0 & \cdots & N_8 & 0 & 0 \\ 0 & N_1 & 0 & 0 & N_2 & 0 & 0 & N_3 & 0 & \cdots & 0 & N_8 & 0 \\ 0 & 0 & N_1 & 0 & 0 & N_2 & 0 & 0 & N_3 & \cdots & 0 & 0 & N_8 \end{array} \right] \left\{ \begin{array}{c} d_{x1} \\ d_{y1} \\ d_{z1} \\ \vdots \\ d_{x8} \\ d_{y8} \\ d_{z8} \end{array} \right\} = \mathbf{N}\left\{\mathbf{d}\right\} \tag{28}$$

The stiffness matrix for the hexahedral element is obtained from the discretization of the second integral term of the weak form on the right hand side.

$$\int_{\Omega_e} \mathbf{\Pi} \nabla N_i dV_0 = \int_{\Omega_e} \boldsymbol{F}\boldsymbol{S} \nabla N_i dV_0 = \int_{\Omega_e} (\mathbf{I} + \nabla \mathbf{d}) \boldsymbol{S} \nabla N_i dV_0 \tag{29}$$

The operation of the second Piola-Kirchhoff stress tensor on ∇N_i is written as

$$\boldsymbol{S}\,\nabla N_i = \left[\begin{array}{cccccc} \dfrac{\partial N_i}{\partial x} & 0 & 0 & \dfrac{\partial N_i}{\partial y} & \dfrac{\partial N_i}{\partial z} & 0 \\ 0 & \dfrac{\partial N_i}{\partial y} & 0 & \dfrac{\partial N_i}{\partial x} & 0 & \dfrac{\partial N_i}{\partial z} \\ 0 & 0 & \dfrac{\partial N_i}{\partial z} & 0 & \dfrac{\partial N_i}{\partial x} & \dfrac{\partial N_i}{\partial y} \end{array} \right] \left\{ \begin{array}{c} S_{xx} \\ S_{yy} \\ S_{zz} \\ S_{xy} \\ S_{xz} \\ S_{yz} \end{array} \right\} = \left[\mathbf{B}_i\right]^\top \left\{\mathbf{S}\right\} \tag{30}$$

Then the integral equation for the stiffness matrix can be obtained as

$$\int_{\Omega_e} \mathbf{\Pi} \nabla N_i dV_0 \quad = \quad \int_{\Omega_e} (\mathbf{I} + \nabla \mathbf{d}) [\mathbf{B}_i]^\top \left\{\mathbf{S}\right\} dV_0 \tag{31}$$

where

$$(\mathbf{I} + \nabla \mathbf{d})[\mathbf{B}_i]^\top = [\mathbf{B}_i]^\top + \nabla \mathbf{d}[\mathbf{B}_i]^\top = [\mathbf{B}_i]^\top + [\mathbf{B}_i]_{NL}^\top \tag{32}$$

The second Piola-Kirchhoff stress tensor is also given by

$$\left\{ \begin{array}{c} S_{xx} \\ S_{yy} \\ S_{zz} \\ S_{xy} \\ S_{xz} \\ S_{yz} \end{array} \right\} = \left[\begin{array}{cccccc} \lambda + 2\mu & \lambda & \lambda & 0 & 0 & 0 \\ \lambda & \lambda + 2\mu & \lambda & 0 & 0 & 0 \\ \lambda & \lambda & \lambda + 2\mu & 0 & 0 & 0 \\ 0 & 0 & 0 & \mu & 0 & 0 \\ 0 & 0 & 0 & 0 & \mu & 0 \\ 0 & 0 & 0 & 0 & 0 & \mu \end{array} \right] \left\{ \begin{array}{c} E_{xx} \\ E_{yy} \\ E_{zz} \\ 2E_{xy} \\ 2E_{xz} \\ 2E_{yz} \end{array} \right\} = [\mathbf{C}]\{\mathbf{E}\} \tag{33}$$

The Green-Lagrange strain tensor can be written as

$$\mathbf{E} = \frac{1}{2}\left[\mathbf{F}^\top \mathbf{F} - \mathbf{I}\right] = \frac{1}{2}\left[\nabla \mathbf{d}^\top + \nabla \mathbf{d} + \nabla \mathbf{d}^\top \nabla \mathbf{d}\right] \tag{34}$$

Defining the displacement field in terms of the nodal displacements using equation (28), the Green-Lagrange strain tensor in vector form in equation (33) may be obtained as follows

$$\{\mathbf{E}\} = \left[[\mathbf{B}] + \frac{1}{2}[\mathbf{B}]_{NL}\right]\{\mathbf{d}\} \tag{35}$$

Hence, the element stiffness matrix will be obtained as

$$\mathbf{K}_{(e)} \quad = \quad \int_{\Omega_e} \left[[\mathbf{B}] + [\mathbf{B}]_{NL}\right]^\top [\mathbf{C}] \left[[\mathbf{B}] + \frac{1}{2}[\mathbf{B}]_{NL}\right] dV_0 \tag{36}$$

It should be noted that we do not use the Newton's method in here due to excessive memory demand in three-dimension. The element mass matrix is obtained from the inertial term in the equation (27) by substituting the nodal displacements in equation (28)

$$\mathbf{M}_{(e)} = \int_{\Omega_e} \rho_0 \mathbf{N}^T \mathbf{N} dV_0 \tag{37}$$

Finally, the boundary loads are imposed on the face of the surface elements by the surface integral term given in the equation (27)

$$\oint_{\partial\Omega_e} N_i \begin{bmatrix} \Pi_{xx} & \Pi_{xy} & \Pi_{xz} \\ \Pi_{yx} & \Pi_{yy} & \Pi_{yz} \\ \Pi_{zx} & \Pi_{zy} & \Pi_{zz} \end{bmatrix} \begin{Bmatrix} n_x \\ n_y \\ n_z \end{Bmatrix} dS_0 = \oint_{\partial\Omega_e} N_i \begin{bmatrix} \sigma_{xx} & \sigma_{xy} & \sigma_{xz} \\ \sigma_{yx} & \sigma_{yy} & \sigma_{yz} \\ \sigma_{zx} & \sigma_{zy} & \sigma_{zz} \end{bmatrix} \begin{Bmatrix} \hat{n}_x \\ \hat{n}_y \\ \hat{n}_z \end{Bmatrix} dS \tag{38}$$

where $\hat{\mathbf{n}}$ is the surface normal vector given in the deformed solid domain

$$\hat{\mathbf{n}} = \hat{n}_x\mathbf{i} + \hat{n}_y\mathbf{j} + \hat{n}_z\mathbf{k} \tag{39}$$

Then the following equilibrium equation is applied at the common fluid-structure interaction boundary

$$\sigma_s\hat{\mathbf{n}}_s = -\sigma_f\hat{\mathbf{n}}_f \tag{40}$$

Upon assembly of the element matrices, the following dynamic system of equations can be obtained for the structure.

$$\mathbf{M}\ddot{\mathbf{d}} + \mathbf{R}(\mathbf{d}) = \mathbf{F} \tag{41}$$

where $\mathbf{M}$, $\mathbf{R}(\mathbf{d})$ and $\mathbf{F}$ are the global mass matrix, nonlinear residual due to material stiffness and load vector, respectively.

Generalized$-\alpha$ Method

In the present approach the system given in (41) is solved using the generalized$-\alpha$ method of [Chung and Hulbert, 1993]. The generalized$-\alpha$ method is an implicit, onestep time integration scheme based on Newmark like approximations [Newmark, 1959] in the time domain and the modified form of the equation of motion becomes

$$\mathbf{M}\ddot{\mathbf{d}}_\alpha + \mathbf{R}(\mathbf{d}_\alpha) = \mathbf{F}_\alpha \tag{42}$$

The method relies on the following interpolations that relate positions, velocities, and accelerations:

$$\mathbf{d}_{n+1} = \mathbf{d}_n + \Delta t\dot{\mathbf{d}}_n + \frac{\Delta t^2}{2}\left[(1-2\beta)\,\ddot{\mathbf{d}}_n + 2\beta\ddot{\mathbf{d}}_{n+1}\right] \tag{43}$$

$$\dot{\mathbf{d}}_{n+1} = \dot{\mathbf{d}}_n + (1-\gamma)\,\Delta t\ddot{\mathbf{d}}_n + \gamma\Delta t\ddot{\mathbf{d}}_{n+1} \tag{44}$$

The acceleration term is solved from equations (43) and then inserted into the equation (44). The modified equations can be written as

$$\ddot{\mathbf{d}}_{n+1} = \frac{1}{\beta\Delta t^2}\left(\mathbf{d}_{n+1} - \mathbf{d}_n\right) - \frac{1}{\beta\Delta t}\dot{\mathbf{d}}_n - \left(\frac{1}{2\beta} - 1\right)\ddot{\mathbf{d}}_n \tag{45}$$

$$\dot{\mathbf{d}}_{n+1} = \frac{\gamma}{\beta\Delta t}\left(\mathbf{d}_{n+1} - \mathbf{d}_n\right) - \left(\frac{\gamma}{\beta} - 1\right)\dot{\mathbf{d}}_n - \left(\frac{\gamma}{2\beta} - 1\right)\Delta t \tag{46}$$

where β and γ are the Newmark parameters. Subscripts α denote evaluation of the respective quantities within the time interval

$$\ddot{\mathbf{d}}_\alpha = (1-\alpha_M)\,\ddot{\mathbf{d}}_n + \alpha_M\ddot{\mathbf{d}}_{n+1} \tag{47}$$

$$\mathbf{R}_\alpha = (1-\alpha_F)\,\mathbf{R}(\mathbf{d}_n) + \alpha_F\mathbf{R}(\mathbf{d}_{n+1}) \tag{48}$$

$$\mathbf{F}_\alpha = (1-\alpha_F)\,\mathbf{F}(\mathbf{d}_n) + \alpha_F\mathbf{F}(\mathbf{d}_{n+1}) \tag{49}$$

Substituting for the displacement and acceleration at time level $n+1$, the following system of equations is obtained

$$\alpha_M\frac{1}{\beta\Delta t^2}\mathbf{M}\mathbf{d}_{n+1} + \alpha_F\mathbf{R}(\mathbf{d}_{n+1}) - \alpha_F\mathbf{F}(\mathbf{d}_{n+1})$$
$$= (1-\alpha_F)\mathbf{F}(\mathbf{d}_n) - (1-\alpha_F)\mathbf{R}(\mathbf{d}_n) - (1-\alpha_M)\mathbf{M}\ddot{\mathbf{d}}_n + \alpha_M\mathbf{M}\left[\frac{1}{\beta\Delta t^2}\mathbf{d}_n + \frac{1}{\beta\Delta t}\dot{\mathbf{d}}_n + \left(\frac{1}{2\beta} - 1\right)\ddot{\mathbf{d}}_n\right] \tag{50}$$

The resulting scheme is second order accurate and an appropriate selection of the involved time integration parameters allow for unconditional stable solutions of nonlinear dynamics. The classical Newmark method can be derived for $\alpha_M = \alpha_F = 1$.

Mesh Deformation Algorithm

There has been extensive research on mesh deformation techniques in the literature and many different mesh deformation algorithms have been proposed for FSI problems in order to compute the displacement of the internal fluid points as the boundaries of a computational domain translate, rotate and deform in order to maintain mesh quality and validity. The mesh deformation techniques include the spring analogy [Batina, 1990], the elastic medium analogy [Johnson and Tezduyar, 1994], the remeshing algorithm [Johnson and Tezduyar, 1999], the radial basis function (RBF) interpolation algorithm [A. de Boer and Bijl, 2007] and the edge swapping algorithm [Dai and Schmidt, 2005]. These approaches are generally requires either the solution of large linear systems or expensive mesh modification algorithms in three-dimension. Therefore, an efficient mesh-deformation strategy based on an algebraic method [Gerhold and Neumann, 2008] is utilized. In the current approach, the displacement of interior fluid nodes is calculated using the negative exponent of the distance function from the fluid-structure interface and the displacement vector at the nearest solid vertex node. The main advantage of the present algebraic method is that it leads to a very sparse algebraic equation (two non-zero entries per row) which is very important for the efficiency of the overall algorithm.

Coupled System of Equations

When the fluid and structure solvers are coupled with the interface conditions given in section and the mesh deformation algorithm described in section , the following linear algebraic system of equations are reached.

$$\left[\begin{array}{cc|c|cc|c} A_{uu} & A_{uu_\Gamma} & A_{uq} & 0 & 0 & A_{up} \\ 0 & A_{u_\Gamma u_\Gamma} & 0 & 0 & A_{ud_\Gamma} & 0 \\ \hline 0 & 0 & A_{qq} & 0 & A_{qd_\Gamma} & 0 \\ \hline 0 & 0 & 0 & A_{dd} & A_{dd_\Gamma} & 0 \\ A_{d_\Gamma u} & A_{d_\Gamma u_\Gamma} & 0 & A_{d_\Gamma d} & A_{d_\Gamma d_\Gamma} & A_{d_\Gamma p} \\ \hline A_{pu} & A_{pu_\Gamma} & 0 & 0 & 0 & 0 \end{array}\right] \left[\begin{array}{c} \mathbf{u} \\ \mathbf{u}_\Gamma \\ \hline \mathbf{q} \\ \hline \mathbf{d} \\ \mathbf{d}_\Gamma \\ \hline p \end{array}\right] = \left[\begin{array}{c} b_1 \\ 0 \\ \hline 0 \\ \hline b_4 \\ b_5 \\ \hline 0 \end{array}\right] \tag{51}$$

where Γ represents the variables at the common fluid-structure interface, $\mathbf{q}$ is the amount of mesh deformation within the fluid domain. These equations can be written as:

$$\left[\begin{array}{cccc} A_{uu} & A_{uq} & A_{ud} & A_{up} \\ 0 & A_{qq} & A_{qd} & 0 \\ A_{du} & 0 & A_{dd} & A_{dp} \\ A_{pu} & 0 & 0 & 0 \end{array}\right] \left[\begin{array}{c} \mathbf{u} \\ \mathbf{q} \\ \mathbf{d} \\ p \end{array}\right] = \left[\begin{array}{c} d_1 \\ 0 \\ d_3 \\ 0 \end{array}\right] \tag{52}$$

In practice, the solution of equation (52) does not converge very quickly and it is rather difficult to construct robust preconditioners for the whole coupled system because of the zero-block diagonal resulting from the divergence-free constraint. In the present paper, we use an upper triangular right preconditioner which results in a scaled discrete Laplacian instead of a zero block in the original system. Then the modified system becomes

$$\left[\begin{array}{cccc} A_{uu} & A_{uq} & A_{ud} & A_{up} \\ 0 & A_{qq} & A_{qd} & 0 \\ A_{du} & 0 & A_{dd} & A_{dp} \\ A_{pu} & 0 & 0 & 0 \end{array}\right] \left[\begin{array}{cccc} I & 0 & 0 & A_{up} \\ 0 & I & 0 & 0 \\ 0 & 0 & I & 0 \\ 0 & 0 & 0 & I \end{array}\right] = \left[\begin{array}{ccc} A_{uu} & A_{uq} & A_{ud} & A_{uu}A_{up} + A_{up} \\ 0 & A_{qq} & A_{qd} & 0 \\ A_{du} & 0 & A_{dd} & A_{du}A_{up} + A_{dp} \\ A_{pu} & 0 & 0 & A_{pu}A_{up} \end{array}\right] \tag{53}$$

and the zero block is replaced with $-A_{pu}A_{up}$, which is a scaled discrete Laplacian. Unfortunately, this leads to a significant increase in the number of non-zero elements due to the matrix-matrix multiplication. However, it is possible to replace the $-A_{up}$ block matrix in the upper triangular right preconditioner with a computationally less expensive matrix, $-\hat{A}_{up}$. The calculations indicate that the largest contribution for the pressure gradients in the momentum equations comes from the right and left elements that share the common face where the components of the velocity vector are discretized. Therefore, we will use the contribution from these two elements for the $-\hat{A}_{up}$ matrix which leads maximum three non-zero entries per row. Although, this approximation does not change the convergence rate of an iterative solver significantly, it leads to a significant reduction in the computing time and memory requirement. The present one-level iterative solver is based on the restricted additive Schwarz method with the FGMRES(m) algorithm [Saad, 1993]. Since the zero block is removed, a block-incomplete factorization, ILU(k), coupled with the reverse Cuthill-McKee ordering [Cuthill and McKee, 1969] can be used within each partitioned sub-domains. The implementation of the preconditioned Krylov subspace algorithm, matrix-matrix multiplication and the restricted additive Schwarz preconditioner were carried out using the PETSc [Balay et al., 2012] software package developed at the Argonne National Laboratories. The computational domain is decomposed into a set of sub-domains or partitions using the METIS library [Karypis and Kumar, 1998].

NUMERICAL RESULTS

In this section, the proposed FSI algorithm is validated for an unsteady Newtonian fluid interacting with an elastic rectangular bar behind a circular cylinder, and a pulsatile flow in a flexible tube, which mimics the case of pulsatile blood flow through elastic arteries.

Test Case I: An Elastic Bar Behind a Rigid Cylinder

The first benchmark case corresponds to the FSI benchmark problem proposed by [Turek and Hron, 2006]. The problem consists of an elastic bar behind a rigid circular cylinder which is placed asymmetrically between two parallel lateral walls as shown in Figure 2. The parameters $H = 0.41$ is the 2D channel height, $L = 2.5$ is the channel length, $D = 0.1$ is the cylinder diameter, $l = 0.35$ is the bar length and $h = 0.02$ is the bar height. The cylinder is positioned at (0.2,0.2) from the left bottom corner of the channel. The control point A is attached to the structure and moving in time starting from the location (0.6,0.2). The time-dependent inflow velocity boundary condition is given by

$$u(y,t) = 1.5\langle U\rangle \frac{y(H-y)}{(H/2)^2} F(t) = 1.5\langle U\rangle \frac{4.0}{0.1681} y(0.41-y)F(t) \tag{54}$$

where $\langle U\rangle$ is the mean inflow velocity and $F(t)$ is given by

$$F(t) = \begin{cases} \frac{1-cos(\pi t/2)}{2} & \text{if } t < 2 \\ 1 & \text{otherwise} \end{cases} \tag{55}$$

The outlet boundary conditions are set to natural (traction-free) boundary conditions:

$$\frac{\partial u}{\partial x} = p, \qquad \frac{\partial v}{\partial x} = 0 \tag{56}$$

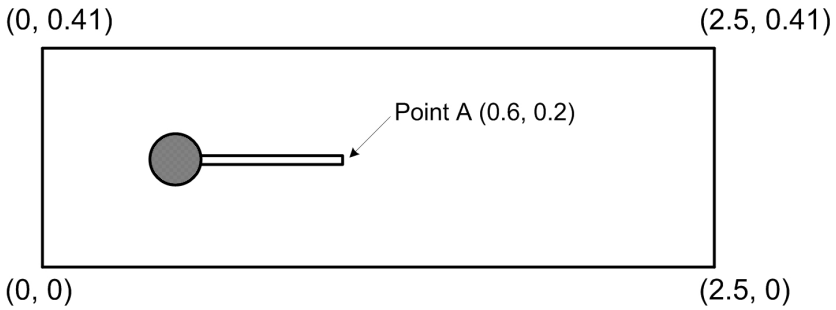

Figure 2: The geometric description of the first validation case.

Table 1: Fluid and structure properties for test case I

		FSI-1	FSI-3
Fluid	Density ρ_f	1000	1000
	Kinematic viscosity ν_f	1×10^{-3}	1×10^{-3}
	Mean Inflow velocity $\langle U\rangle$	0.2	2
Solid	Density ρ_s	1000	1000
	Poisson ratio ν_s	0.4	0.4
	Shear modulus μ_s	0.5×10^6	2×10^6

The physical parameters for the compressible Saint Venant-Kirchhoff material and the incompressible Navier-Stokes equations are provided in Table 1 for the FSI-1 and FSI-3 problems proposed in the work of [Turek and Hron, 2006]. The proposed FSI-1 corresponds a steady state solution with a Reynolds number of 20, meanwhile FSI-3 results in a periodic solution with a Reynolds number of 200. For this benchmark problem, three different mesh resolutions are employed: the coarse mesh M1 with $8,736$ vertices and $8,496$ quadrilateral elements (54,656 DOF), the medium mesh M2 with $33,072$ vertices and $32,592$ quadrilateral elements (206,352 DOF)

and the fine mesh M3 with $128,484$ vertices and $127,524$ quadrilateral elements (800,444 DOF). The successive meshes are generated by multiplying the mesh size by a factor of 0.5 in each direction. The meshes are generated using the paving algorithm within the CUBIT [Blacker et al., 1999] mesh generation environment and the meshes is highly refined close to the solid surfaces using local mesh refinement algorithms. The constant time step is set to 5×10^{-4} and the calculations are started from the rest. The time variation of vertical displacement for the FSI-1 and FSI-3 problems at the point A at the tip of the bar are tabulated in the Table 2 and Table 3, respectively, and the values are compared with the several other results available in the literature. The present results are in relatively good agreement with the results in the literature and the calculations can correctly predict the amplitude of the oscillations. In particular, the difference in the magnitude of the $y-$displacement value of [Richter and Wick, 2010] is less than 0.13% for the FSI-1 case. The time variation of vertical displacement for the FSI-3 problem at the point A at the tip of the bar is given in Figure 3 on the meshes M1−M3. The vertical displacement of the point A settles into a periodic state with a period of 0.182 after several cycles. Although the computed $y-$displacements on the meshes M1−M3 are comparable with each other, there is a slight decrease in the amplitude of the oscillations for the mesh M1 due to a relatively coarse mesh resolution. The computed $u-$velocity vector components for the FSI-3 problem are shown in Figure 4 with the streamlines at several different time levels corresponding to the maximum, zero and minimum $y-$displacement of the point A. The streamlines indicate an alternating large recirculation zone just behind the cylinder.

Table 2: Displacements at point A for FSI-1 ($Re = 20$) of test case I.

	DOF	d_x [$\times 10^{-3}$]	d_y [$\times 10^{-3}$]
Present FSI solver (M1)	$54,656$	0.022217	0.78201
Present FSI solver (M2)	$206,352$	0.022349	0.81091
Present FSI solver (M3)	$800,444$	0.022490	0.81659
[Turek and Hron, 2006]	$304,128$	0.022732	0.82071
[Degroote et al., 2010]	$320,372$	0.022651	0.83478
[Richter and Wick, 2010]	$351,720$	0.022695	0.81556

Table 3: Displacements at point A for FSI-3 ($Re = 200$) of test case I.

	DOF	d_x [$\times 10^{-3}$]	d_y [$\times 10^{-3}$]
Present FSI solver (M1)	$54,656$	-2.573 ± 2.449	$+1.473 \pm 32.777$
Present FSI solver (M2)	$206,352$	-2.823 ± 2.671	$+1.453 \pm 34.603$
Present FSI solver (M3)	$800,444$	-2.882 ± 2.722	$+1.452 \pm 34.995$
[Turek and Hron, 2006]	$304,128$	-2.69 ± 2.53	$+1.48 \pm 34.38$
[Wick, 2011]	$72,696$	-2.84 ± 2.67	$+1.28 \pm 34.61$
[Chabannes et al., 2013]	$95,427$	-2.88 ± 2.75	$+1.35 \pm 34.72$

Test Case II: A Pressure-pulse Propagating in a Flexible Tube

As a final benchmark problem, we consider the three-dimensional transient FSI problem proposed by [Gerbeau and Vidrascu, 2003], which has been considered by many authors [Küttler and Wall, 2008; Formaggia et al., 2001; Gee et al., 2011; Malan and Oxtoby, 2013]. The problem is related to the blood flow through elastic arteries and the test configuration consists of an incompressible viscous flow through a flexible circular tube with an inner radius of $0.5\,cm$, a length of $5\,cm$ and a wall thickness of $0.1\,cm$. The tube wall is clamped at both ends and a pressure boundary condition is imposed on the fluid at the inflow and outflow boundaries. The fluid is initially at rest and a pressure of $1.3 \times 10^{-4}\,dyn/cm^2$ is imposed on the inflow boundary for $t < 0.003\,s$, while at the outflow boundary, the pressure is set to zero throughout the analysis. The physical properties for the compressible Saint Venant-Kirchhoff material and the incompressible Newtonian fluid used for the third benchmark cas are listed in Table 4. The computational mesh used for this benchmark case is shown in Figure 5 and the mesh is highly clustered next to the fluid-structure interface. The mesh consists of $270,300$ hexahedral elements and $278,154$ vertices leading to 2,557,571 DOF for the whole domain. The

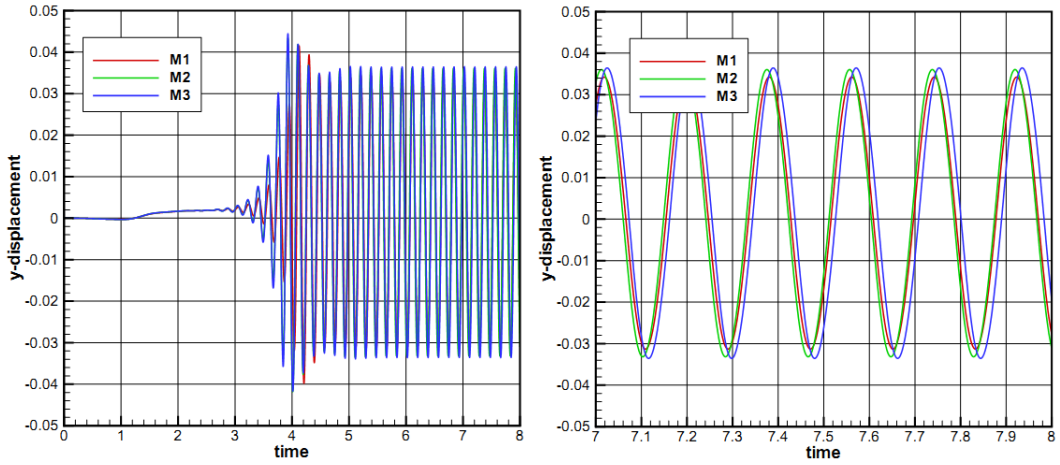

Figure 3: The time variation of vertical displacement for an elastic bar behind a rigid cylinder at $Re = 200$.

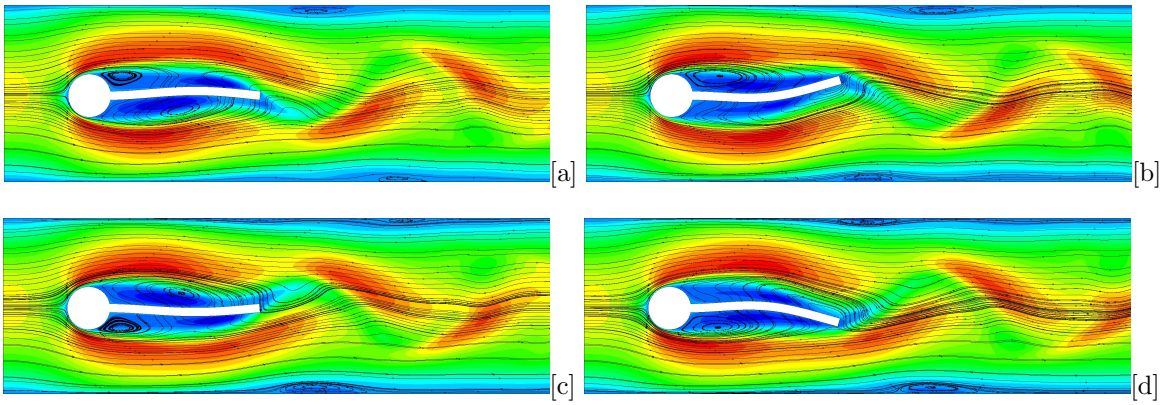

Figure 4: The computed $u-$velocity vector component contours with the streamlines for an elastic bar behind a rigid cylinder at $t = 8.072$ [a], $t = 8.117$ [b], $t = 8.165$ [c] and $t = 8.208$ [d] at $Re = 200$.

mesh shown in Figure 5 for this test case consists of $270,300$ hexahedral elements and $278,154$ vertices leading to 2,557,571 DOF for the whole computational domain. The mesh is highly clustered near the fluid-structure interface and we used 101 vertices along the tube axis. Throughout the computations, the time step is set to 1×10^{-4} with the first-order Euler implicit in the fluid domain in order to be consistent with the earlier result of [Gee et al., 2011]. In Figure 6, the time variations of the radial components of displacement and velocity on the inner wall halfway along the pipe are presented for the first $0.02s$ of motion. The snapshot of the computed deformation contours at $0.0069s$ is given in Figure 7, which is comparable with the structural deformation result of [Gee et al., 2011]. It should be noted that the wall deformations presented in Figure 7 are exaggerated by a factor of 10 for clarity. The $u-$velocity profiles at several different locations including the mid-plane are shown in Figure 8 at the same time level. The velocity profile at $x = -2\,cm$ shows backward flow meanwhile the other locations indicate the mean flow in the positive $x-$direction. We should mention that the present benchmark is a rather difficult one due to the impulsive started incompressible viscous flow which leads to extremely high shear forces on the walls at startup and a very thin boundary layer with reverse flows as seen in Figure 8. The calculations with smaller time steps and the second-order Euler implicit in the fluid domain show that the current results are far from the converged solution.

Table 4: Fluid and structure properties for test case II

Fluid		Structure	
Density	$\rho_f = 1\, g/cm^3$	Density	$\rho_s = 1.2\, g/cm^3$
Dynamic viscosity	$\mu_f = 3 \times 10^{-2}\, g/cm \cdot s$	Poisson ratio	$\nu_s = 0.3$
		Young modulus	$E_s = 3 \times 10^6$

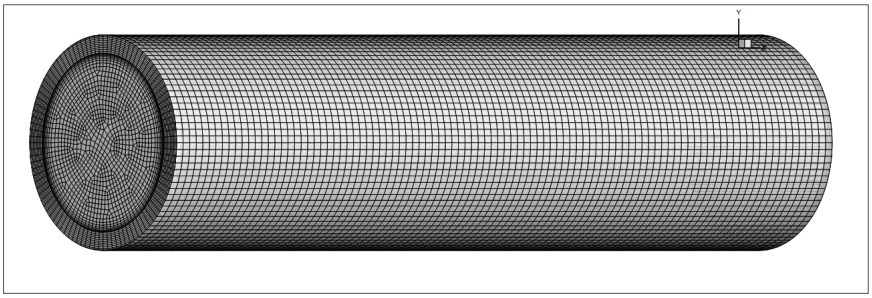

Figure 5: The computational unstructured hexahedral mesh for both the fluid and solid domains.

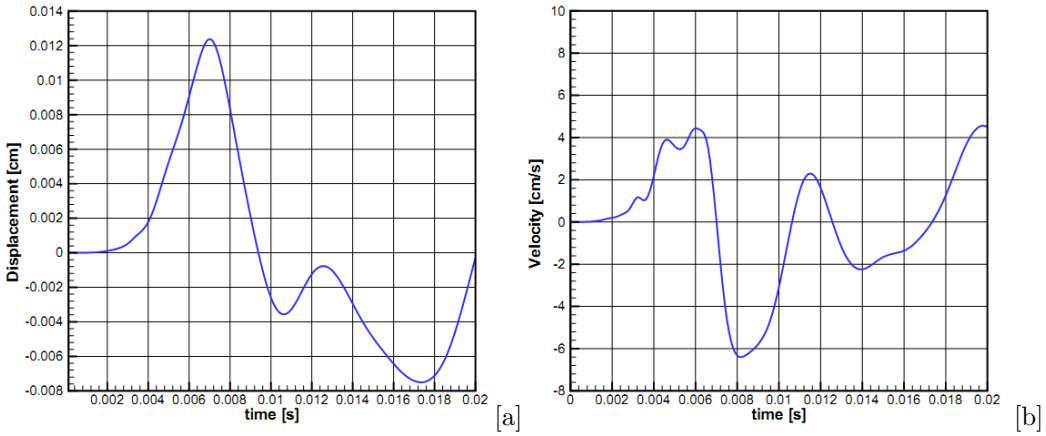

[a] [b]

Figure 6: The radial components of displacement and velocity on the inner wall halfway along the pipe.

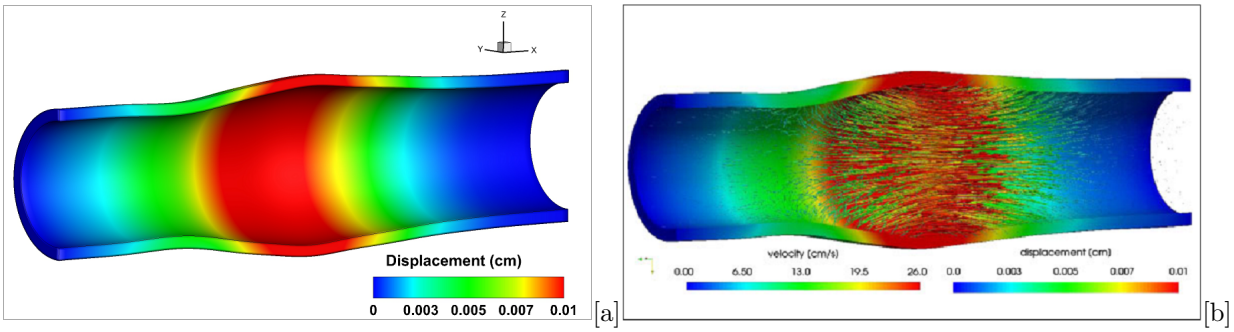

[a] [b]

Figure 7: The computed radial displacement contours at $t = 0.0069s$ for the present calculations [a] and results of [Gee et al., 2011] [b]. The wall deformations are exaggerated by a factor of 10 for clarity.

CONCLUSIONS

A new algorithm based on the ALE formulation has been developed for a fully coupled solution of the large-scale fluid-structure interaction problems where the fluid is modeled by the incompressible Navier-Stokes equations and the structure is modeled by the compressible Saint Venant-Kirchhoff model. The numerical formulation uses the staggered arrangement of the primitive variables in order to avoid odd-even pressure decoupling or spurious pressure modes on unstructured meshes. The continuity equation is satisfied within each element exactly and the summation of the continuity equations can be exactly reduced to the domain boundary, which

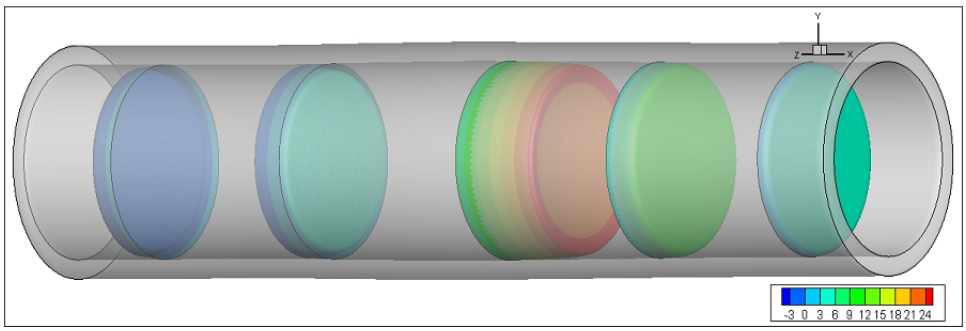

Figure 8: The computed $u-$velociy profiles at several different locations: $x = -2\,cm$, $-1\,cm$, $0\,cm$, $1\,cm$ and $2\,cm$.

is important for the global mass conservation. A special attention is also given to satisfy the Discrete Geometric Conservation Law (DGCL) on moving meshes at discrete level. The governing equations of the solid domain is discretized using the classical Galerkin finite element in a Lagrangian frame. The resulting large-scale algebraic linear equations from the discretization of fluid and solid domains are solved in a fully coupled form using a monolithic approach based on a one-level restricted additive Schwarz preconditioner with a block-incomplete factorization within each partitioned sub-domains. The present algorithm is validated for a two-dimensional and a three-dimensional fluid-structure interaction benchmark problem with comparisons to the results in the literature. In the future, we will combine the present approach with the two-level approach in [Sahin, 2011] in order to further improve the efficiency of the present monolithic approach.

ACKNOWLEDGMENTS

The authors acknowledge financial support from Turkish National Scientific and Technical Research Council (TUBITAK) through project number 112M107. The authors also gratefully acknowledge the use of the Chimera machine at the Faculty of Aeronautics and Astronautics at ITU, the computing resources provided by the National Center for High Performance Computing of Turkey (UYBHM) under grant number 10752009 and the computing facilities at TUBITAK ULAKBIM, High Performance and Grid Computing Center.

References

A. de Boer, M. S. v. d. S. and Bijl, H. (2007). Mesh deformation based on radial basis function interpolation. *Comput. Struct.*, 85:784–795.

Anderson, W. K. and Bonhaus, D. L. (1994). An implicit upwind algorithm for computing turbulent flows on unstructured grids. *Comput. Fluids*, 23(1):1–21.

Balay, S., Brown, J., , Buschelman, K., Eijkhout, V., Gropp, W. D., Kaushik, D., Knepley, M. G., McInnes, L. C., Smith, B. F., and Zhang, H. (2012). PETSc users manual. Technical Report ANL-95/11 - Revision 3.3, Argonne National Laboratory.

Barker, A. T. and Cai, X.-C. (2010). Scalable parallel methods for monolithic coupling in fluid-structure interaction with application to blood flow modeling. *J. Comput. Phys.*, 229:642–659.

Barth, T. J. (1991). A 3-D upwind Euler solver for unstructured meshes. Technical Report Paper 91-1548-CP, AIAA.

Batina, J. T. (1990). Unsteady Euler airfoil solutions using unstructured dynamic meshes. *AIAA J.*, 28(8):1381–1388.

Behr, M. and Tezduyar, T. E. (1994). Finite element solution strategies for large-scale flow simulations. *Comput. Meth. Appl. Mech. Engrg.*, 112(14):3–24.

Blacker, T. D., Benzley, S., Jankovich, S., Kerr, R., Kraftcheck, J., Kerr, R., Knupp, P., Leland, R., Melander, D., Meyers, R., Mitchell, S., Shepard, J., Tautges, T., and White, D. (1999). CUBIT mesh generation enviroment users manual: Volume 1. Technical report, Sandia National Laboratories, Albuquerque, NM.

Chabannes, V., Pena, G., and Prudhomme, C. (2013). High-order fluid-structure interaction in 2D and 3D application to blood flow in arteries. *J. Comput. Appl. Math.*, 246:1–9.

Chung, J. and Hulbert, G. M. (1993). A time integration algorithm for structural dynamics with improved numerical dissipation: The generalized-α method. *J. Appl. Mech.*, 60:371.

Cuthill, E. and McKee, J. (1969). Reducing the bandwidth of sparse symmetric matrices. In *Proceedings of the 1969 24th national conference*, ACM '69, pages 157–172, New York, NY, USA. ACM.

Dai, M. and Schmidt, D. P. (2005). Adaptive tetrahedral meshing in free-surface flow. *J. Comput. Phys.*, 208(1):228–252.

Degroote, J., Haelterman, R., Annerel, S., Bruggeman, P., and Vierendeels, J. (2010). Performance of partitioned procedures in fluid-structure interaction. *Comput. Struct.*, 88(78):446–457.

Degroote, J. and Vierendeels, J. (2011). Multi-solver algorithms for the partitioned simulation of fluid-structure interaction. *Comput. Meth. Appl. Mech. Engrg.*, 200(2528):2195–2210.

Donea, J., Giuliani, S., and Halleux, J. (1982). An arbitrary Lagrangian-Eulerian finite element method for transient dynamic fluid-structure interactions. *Comput. Meth. Appl. Mech. Engrg.*, 33(13):689–723.

Formaggia, L., Gerbeau, J. F., Nobile, F., and Quarteroni, A. (2001). On the coupling of 3D and 1D Navier-Stokes equations for flow problems in compliant vessels. *Comp. Meth. Appl. Mech. Engrg.*, 191(67):561–582.

Gee, M. W., Küttler, U., and Wall, W. A. (2011). Truly monolithic algebraic multigrid for fluid-structure interaction. *Int. J. Numer. Meth. Eng.*, 85(8):987–1016.

Gerbeau, J.-F. and Vidrascu, M. (2003). A quasi-Newton Algorithm based on a reduced model for fluid-structure interaction problems in blood flows. *ESAIM-Math. Model. Num.*, 37:631–647.

Gerhold, T. and Neumann, J. (2008). *The Parallel Mesh Deformation of the DLR TAU-Code*, volume 96 of *Notes on Numerical Fluid Mechanics and Multidisciplinary Design (NNFM)*, chapter 20, pages 162–169. Springer Berlin Heidelberg.

Geuzaine, P., Grandmont, C., and Farhat, C. (2003). Design and analysis of ALE schemes with provable second-order time-accuracy for inviscid and viscous flow simulations. *J. Comput. Phys.*, 191(1):206–227.

Harlow, F. H. and Welch, J. E. (1965). Numerical calculation of time-dependent viscous incompressible flow of fluid with free surface. *Phys. Fluids*, 8:2182–2189.

Hirt, C., Amsden, A., and Cook, J. (1974). An arbitrary Lagrangian-Eulerian computing method for all flow speeds. *J. Comput. Phys.*, 14(3):227–253.

Hughes, T. J., Liu, W. K., and Zimmermann, T. K. (1981). Lagrangian-Eulerian finite element formulation for incompressible viscous flows. *Comput. Meth. Appl. Mech. Engrg.*, 29(3):329–349.

Johnson, A. and Tezduyar, T. (1994). Mesh update strategies in parallel finite element computations of flow problems with moving boundaries and interfaces. *Comput. Meth. Appl. Mech. Engrg.*, 119(12):73–94.

Johnson, A. A. and Tezduyar, T. E. (1999). Advanced mesh generation and update methods for 3D flow simulations. *Comput. Mech.*, 23:130–143.

Karypis, G. and Kumar, V. (1998). A fast and high quality multilevel scheme for partitioning irregular graphs. *SIAM J. Sci. Comput.*, 20(1):359–392.

Küttler, U., Gee, M., Förster, C., Comerford, A., and Wall, W. A. (2010). Coupling strategies for biomedical fluidstructure interaction problems. *Int. J. Numer. Meth. Bio.*, 26(3-4):305–321.

Küttler, U. and Wall, W. A. (2008). Fixed-point fluidstructure interaction solvers with dynamic relaxation. *Comput. Mech.*, 43:61–72.

M. Benzi, G. H. G. and Liesen, J. (2005). Numerical solution of saddle point problems. *Acta Numer.*, 14:1–37.

Malan, A. and Oxtoby, O. (2013). An accelerated, fully-coupled, parallel 3D hybrid finite-volume fluidstructure interaction scheme. *Comput. Meth. Appl. Mech. Engrg.*, 253(0):426–438.

Muddle, R. L., Mihajlovic, M., and Heil, M. (2012). An efficient preconditioner for monolithically-coupled large-displacement fluid-structure interaction problems with pseudo-solid mesh updates. *J. Comput. Phys.*, 231(21):7315–7334.

Naderi, A., Darbandi, M., and Taeibi-Rahni, M. (2010). Developing a unified FVE-ALE approach to solve unsteady fluid flow with moving boundaries. *Int. J. Numer. Meth. Fluids*, 63(1):40–68.

Newmark, N. M. (1959). A method of computation for structural dynamics. *J. Eng. Mech. Div.-ASCE*, 85(3):67–94.

Richter, T. and Wick, T. (2010). Finite elements for fluidstructure interaction in ALE and fully Eulerian coordinates. *Comput. Meth. Appl. Mech. Engrg.*, 199(4144):2633–2642.

Saad, Y. (1993). A flexible inner-outer preconditioned GMRES algorithm. *SIAM J. Sci. Comput.*, 14(2):461–469.

Sahin, M. (2011). A stable unstructured finite volume method for parallel large-scale viscoelastic fluid flow calculations. *J. Non-Newton. Fluid*, 166(1415):779–791.

Thomas, P. D. and Lombard, C. K. (1979). Geometric conservation law and its application to flow computations on moving grids. *AIAA J.*, 17:1030–1037.

Turek, S. and Hron, J. (2006). Proposal for numerical benchmarking of fluid-structure interaction between an elastic object and laminar incompressible flow. In Bungartz, H.-J. and Schfer, M., editors, *Fluid-Structure Interaction*, volume 53 of *Lecture Notes in Computational Science and Engineering*, pages 371–385. Springer Berlin Heidelberg.

Wick, T. (2011). Solving monolithic fluid-structure interaction problems in arbitrary Lagrangian Eulerian coordinates with the deal.II library. Technical report, University of Heidelberg, Heidelberg, Germany.